PCCP

ROYAL SOCIETY OF CHEMISTRY

PAPER

View Article Online
View Journal | View Issue

Check for updates

Cite this: *Phys. Chem. Chem. Phys.*, 2025, **27**, 17864

Open Access Article. Published on 01 2568. Downloaded on 1/6/2569 14:33:01.
This article is licensed under a Creative Commons Attribution 3.0 Unported Licence.

A multiscale computational and experimental study of TBA–fluorescent probes for protein sensing: photobasicity over twisted intramolecular charge transfer as a new mechanism for protein induced fluorescence enhancement

Makay T. Murray, [a] Austin Pounder, [a] Ryan E. Johnson,[b] Keenan T. Regan, [b] Richard A. Manderville [b] and Stacey D. Wetmore *[a]

Received 17th May 2025,
Accepted 31st July 2025

DOI: 10.1039/d5cp01851j

rsc.li/pccp

Fluorescent probes are powerful tools for the detection of proteins in biomedical applications. However, the design of selectively active fluorescent probes is challenging due in part to difficulties predicting the functions of novel modifications, especially in different cellular environments. In the present study, a family of cyclic *N*-glycol-linked 4-formyl-aniline probes (denoted AnMeInd, AnMeBtz, and AnBtz), which have distinct thrombin binding affinities and fluorescent responses, were investigated at the T3 position of the thrombin binding aptamer (TBA) using TD-DFT calculations and classical and driven-adaptive bias molecular dynamics (MD) simulations. Classical MD and D-ABMD simulations corroborate the experimentally observed differences in thrombin binding affinities relative to canonical TBA, highlighting that neutral, shorter probes that lack an abundance of exocyclic substituents are better accommodated in a thrombin binding pocket that is rich in aromatic and charged residues. TD-DFT suggests that cationic AnMeInd and AnMeBtz exhibit the same inherent tendency to undergo twisted intramolecular charge transfer (TICT). However, the methyl substituents of AnMeInd reduce probe contacts with the aptamer scaffold to enhance TICT in the unbound state, and adjust probe binding location in the thrombin hydrophobic pocket, which increases solvent shielding, probe rigidity, and TICT suppression upon target binding compared to AnMeBtz. Unlike the cationic analogues, combined computational and experimental data suggest the best AnBtz probe functions as a photobase. Although AnBtz undergoes protonation in the excited state in solvent exposed environments (*i.e.*, unbound TBA), which facilitates nonradiative decay, this pathway is suppressed upon thrombin binding due to reduced solvent accessibility, thereby enhancing fluorescence. These findings underscore the importance of tuning probe charge, linker length, exocyclic substituents, flexibility, and microenvironment in both the unbound and bound states to optimize fluorescence response. Our results provide a strategic foundation for designing high-performance fluorescent probes for biosensing and nucleic acid-based diagnostics.

Introduction

Cardiovascular diseases (CVDs) are currently the leading cause of death in the world.[1] Early diagnosis is the most effective way to identify and monitor individuals at greater risk of CVDs and thereby reduce the impact of severe and fatal diseases.[2] Human α-thrombin is a central serine protease involved in the coagulation cascade that is linked to atherosclerosis,[3] deep vein thrombosis,[4] thrombophilia,[5] and other CVDs.[6] Therefore, thrombin detection is highly relevant for disease prevention and treatment. A promising class of molecules for protein detection is aptamers, which are single-stranded DNA (typically 10–70 nucleotides) that can selectively bind to targets with high affinity, and are associated with manufacturing ease, low immunogenicity, and long shelf-lives.[7] Despite these advantages, aptamers composed of canonical nucleotides lack the ability to report protein binding events. A practical strategy to overcome this limitation is to integrate a fluorogenic probe

[a] *Department of Chemistry and Biochemistry, University of Lethbridge, 4401 University Drive West, Lethbridge, AB T1K 3M4, Canada. E-mail: stacey.wetmore@uleth.ca*
[b] *Department of Chemistry & Toxicology, University of Guelph, 50 Stone Road East, Guelph, ON N1G 2W1, Canada*

 This journal is © the Owner Societies 2025

Open Access Article. Published on 01 2568. Downloaded on 1/6/2569 14:33:01.
This article is licensed under a Creative Commons Attribution 3.0 Unported Licence.

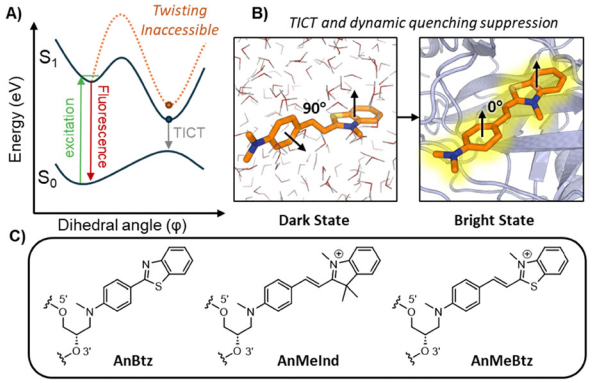

Fig. 1 (A) Illustration of the potential energy surfaces for TICT excited-state molecular twisting and TICT inhibition due to probe intercalation into the protein. (B) Illustration of the TICT 'dark state' in a low viscosity solvent (left) and 'bright state' upon protein binding (right). (C) Molecular structures of the probes considered in this study.

within the nucleotide sequence, which generally retains the canonical three-dimensional fold, and high selectivity and specificity of the unmodified aptamer, and results in a powerful tool for detection in complex media including cellular environments.[8–10] Indeed, fluorogenic probes that selectively activate when in contact with target analytes have significantly advanced chemical and biological analysis.[11]

Protein induced fluorescent enhancement (PIFE) is an extremely useful 'turn-on' mechanism for fluorogenic probe design. Fluorescent molecular rotors (FMRs) that contain flexible, bridged aryl species with electron donor and acceptor moieties, such as cyanines, hemicyanines, and coumarins (among others),[12] can exhibit PIFE due to changes in probe rigidity and/or solvent quenching upon target binding.[13] A key underlying photophysical phenomenon that can give rise to PIFE for FMRs is twisted intramolecular charge transfer (TICT, Fig. 1A).[12] Specifically, upon excitation of an electron to the S_1 state, electron density shifts toward the acceptor moiety, followed by structural relaxation. The new geometrically-relaxed structure in the S_1 state is accessible through free rotation about the bridge, resulting in orthogonal donor and acceptor ring planes. Electronic relaxation ($S_1 \rightarrow S_0$) in this orthogonal conformation goes through a nonradiative decay pathway, quenching fluorescence compared to that emitted from a planar conformation (Fig. 1B). As a result, FMRs demonstrate viscosity-sensitive fluorescence, exhibiting minimal emission in low-viscosity environments (water) and enhanced fluorescence in high-viscosity media (polyethylene glycol, glycerol). In parallel, protein binding can inhibit inter-aryl rotation and promote the (planar) emissive intramolecular charge transfer (ICT) state. The optimum probe design to maximize PIFE is not well understood, necessitating studies on candidate probes with a range of target binding affinities and fluorescence readouts.

The thrombin binding aptamer (TBA) provides an excellent platform for testing probe performance.[8,10,14–17] TBA binds to the fibrinogen recognition site (exosite I) of human α-thrombin with an apparent dissociation constant (K_d) ranging from low- to mid-nanomolar.[18] TBA (5′-GGTTGG-TGT-GGTTGG-3′) folds into a chair-like structure, with two guanine tetrads forming an antiparallel guanine-quadraplex (GQ) topology stabilized by a central potassium ion. Folding results in two parallel TT loops on one TBA face and a TGT loop on the opposing face.[19] TBA binds to the thrombin target *via* the TT loops (T3/T4 and T12/T13), while the TGT loop is solvent exposed. Although the direct incorporation of hemicyanine probes into TBA has already demonstrated considerable success for thrombin detection,[8–10,20] there is room for improvement in probe design. However, *de novo* prediction of the structure–function relationship of aptamers containing a PIFE-based probe, particularly in terms of enhanced target binding affinity and response, is challenging. Although structural information would facilitate our understanding of the intricacies of probe function, only a few X-ray crystal structures of modified TBA bound to thrombin are available to our knowledge,[18,21–26] none of which contain a PIFE-based probe. Furthermore, computational investigations of the structure and function of fluorescent probes incorporated into TBA remain scarce.[8,10,27–29]

In the present work, we investigate modified TBA and TBA–thrombin complexes containing three fluorogenic probes that differ in their charge (neutral and cationic), acceptor ring systems (benzothiazole and indoline), and inter-ring linker (olefin and single bond). Specifically, we investigate AnBtz (2-(4-dimethylaniline)benzothiazole), AnMeInd (2-[4-(dimethylaniline)ethenyl]-1,3,3-trimethyl-3*H*-indolium), and AnMeBtz (2-[4-(dimethylaniline)ethenyl]-3-methylbenzothiazolium; Fig. 1C). These modifications were selected due to the availability of accurate experimental data for the probes incorporated at the T3 position of TBA,[8] which highlight the effects of the probe chemical composition on thrombin binding affinities (K_d), fluorescent absorption/emission ($\lambda_{ex}/\lambda_{em}$) spectra, relative fluorescence intensity upon target binding (I_{rel}), and quantum yield (Φ_f). We have employed molecular dynamics (MD) simulations to unravel the structural dynamics of the probe-modified TBA aptamers in isolation and when bound to thrombin to identify factors responsible for unbound probe quenching and bound probe fluorescent enhancement. Driven-adaptive biased MD (D-ABMD) was used to further explore the relative thrombin binding affinity of the decorated TBAs. Time-dependent density functional theory (TD-DFT) along with experimentally-determined fluorescence intensities of the free probes across a range of solvents were utilized to investigate the inherent FMR characteristics of the probes and thereby rationalize differences in the photophysical responses. Together, these findings provide critical insights into the behavior of probe-modified TBAs and establish key design principles for the future development of improved fluorescent biosensors. By highlighting the roles of charge, linker length, conformational flexibility, and photobasicity in the interplay between TICT and FMR behavior, this study lays the groundwork for the rational development of next-generation fluorogenic aptamer sensors for biomolecular detection.

Open Access Article. Published on 01 2568. Downloaded on 1/6/2569 14:33:01.
This article is licensed under a Creative Commons Attribution 3.0 Unported Licence.

Methodology

MD and D-ABMD force fields

Canonical DNA and protein residues were described using the AMBER OL15[30] and ff14SB force fields,[31] respectively, while water was treated with TIP4P-EW.[32] Ion parameters from Joung and Cheatham were used for Na^+, Cl^-, and K^+.[33] To obtain compatible parameters for the fluorogenic probes, each probe was first built in the *R*-substituted ethylene glycol form using GaussView 6.0.16[34] and subjected to an unguided and exhaustive conformational search using RDKit[35] with the UFF force field.[36] The lowest energy conformers were further refined with B3LYP-D3(BJ)/6-31G(d) optimizations using Gaussian 16 (C.01).[37–40] The resulting structurally-distinct conformers that are related by variations in the dihedral angles in the backbone and donor–acceptor bridge, along with minimized dimethyl phosphate, were used for parameterization with the PyRED server.[41] The parmchk2 tool of AMBER was used to assign GAFF[42] atom types (Table S1). Finally, library files were generated for each probe using tleap. Parameterized probe (.mol2), force field modification (.frcmod), and library (.lib) files are available as SI.

Model building

Starting points for MD simulations were generated from two X-ray crystal structures of canonical TBA bound to thrombin (PDB ID: 4DII and 1HAO), which differ by a 180° rotation about the TBA central axis prior to thrombin binding. Thrombin residue numbering used throughout is based on PDB ID: 4DII. Unresolved residues in the flexible loops and terminal strands of thrombin were added manually using PyMOL 2.5.2[43] (Table S2) and subsequently minimized using the optimize.py plugin for PyMOL. The AnBtz, AnMeInd, and AnMeBtz probes prepared as outlined above were introduced into the T3 position of TBA by aligning the terminal oxygen atoms of the probe (denoted O5′ and O3′ for ease of comparison to DNA, Fig. 1 and Fig. S1) with respect to the corresponding atoms of the T3 nucleotide using the align tool of PyMOL. The preexisting canonical T3 was then deleted and the probe bonded to G2 and T4. Given the numerous internal degrees of freedom in these conjugates, initial probe configurations were considered that orient the probe in the lowest energy co-planar conformation away from the center of mass of TBA along three cardinal directions while avoiding overlap with thrombin by adjusting the glycol backbone (Fig. S2). The unbound TBA systems were similarly constructed, with thrombin deleted before probe incorporation (Fig. S3).

Each TBA/TBA–thrombin model was prepared for simulation using the tLEaP module of AMBER 22.[44] Specifically, each system was solvated in a truncated-octahedral box of TIP4P-EW water,[33] with the nearest box face being a minimum distance of 10 Å from the solute and the probe identity dictating total box size. This added ∼2100–4000 water molecules for each unbound TBA and ∼11 000 water molecules for each TBA–thrombin complex (Table S3). Next, each system was neutralized with Na^+ and then brought to an intracellular physiological NaCl concentration of 150 mM, with ion count determined using the SLTCAP[45] calculator.

MD simulation procedure

Each model was subjected to minimization, heating, and equilibration. First, the system was minimized in four stages: (1) solvent and ions were minimized, while restraining the solute; (2) the hydrogens on the solute were minimized, while restraining the rest of the model; (3) all atoms of the solute were minimized, while restraining the solvent and ions; and (4) the entire system was minimized. Each minimization stage involved 2000 cycles of the steepest descent algorithm followed by 2000 steps of conjugate gradient minimization. At each step, a force constant of 100.0 kcal mol^{-1} $Å^{-2}$ was used as the restraint. Next, heating was carried out to bring the systems from 10 K to 310 K in 50 K increments, using 20 000 steps of heating per increment. The solute was restrained with a 25 kcal mol^{-1} $Å^{-2}$ force constant during heating. Finally, five equilibration steps were performed, while decreasing the restraint on the solute from 20 to 15, 10, 5, and finally 1.5 kcal mol^{-1} $Å^{-2}$. Each of the five equilibration rounds involved 10 000 steps. A final 150 ns equilibration run was performed with pmemd.-cuda. The time step for all minimization, heating, and equilibration stages was 1 fs. The SHAKE[46] algorithm was used during MD production, allowing for a time step of 2 fs.

Bound TBA–thrombin complexes were initially simulated for 1 μs in triplicate for the three distinct probe poses across both crystal structures (Fig. S2). Analysis of the resulting trajectories indicated that the 4DII thrombin–TBA binding orientation is not viable for the probe-modified TBAs and therefore these models were not further considered (see results). Due to the observed high dynamics of all probes in the 1HAO orientation, the corresponding simulations were treated as an extended equilibration step. The trajectories were clustered with respect to the root-mean-square deviation (RMSD) of residues at the aptamer–thrombin interface (defined as G2–G5 and G11–G14 (TBA), and Phe34, Lys36, Gln38, Leu64–Arg67, Tyr76, Arg75–Asn79, and Glu81–Leu86 (thrombin)). The representative structure from the dominant cluster was re-solvated and re-ionized (Table S3) prior to initiating 9 × 1 μs final MD production simulations. For unbound TBA models, 1 μs MD production simulations were performed in triplicate from each of the three initial probe orientations (Fig. S3). All simulations were run as an NPT ensemble at 310 K (Langevin thermostat)[47] and 1 bar (Berendsen barostat).[48] The water density was ∼1 g mL^{-1} and the periodic boundary condition was enabled. Frames from these final production simulations were saved to disk every 20 ps for analysis (a total of 20 000 frames per simulation replica).

MD simulation analysis protocol

MD simulations were analyzed using cpptraj from the AmberTools22 suite and a collection of in-house scripts (available in SI). Analysis was conducted across all replicas of final MD production simulations for each system and reported as averages with standard deviations where appropriate. Trajectories were visually inspected using PyMOL prior to numerical

 This journal is © the Owner Societies 2025

Open Access Article. Published on 01 2568. Downloaded on 1/6/2569 14:33:01.
This article is licensed under a Creative Commons Attribution 3.0 Unported Licence.

analysis. Trajectory analysis included evaluation of the RMSDs of all heavy atoms and peptide/nucleotide backbone atoms (N, C, and CA (peptides) along with P, O5′, C5′, C4′, C3′, and O3′ (nucleotides)), and per-residue root-mean-square fluctuation (RMSF). To verify the integrity of the central guanine tetrads of TBA, K^+ coordination distances to each guanine O6 atom were monitored. Hydrogen-bonding occupancies were evaluated based on a distance cut-off of <3.2 Å and an angle cut-off of $>130^\circ$. Stacking occupancies were calculated based on the distance between the centers of mass of the aromatic rings being <5 Å and the rings having an interplanar angle $<30^\circ$ or $>150^\circ$. The occupancies of T-shaped π–π interactions were calculated using a distance cut-off between the centers of mass of the rings of <5 Å and an interplanar angle between the rings of $>75^\circ$ and $<105^\circ$. The occupancy of edge-on π-interactions were evaluated using a distance cutoff between the donor and the center of mass of the ring of <5 Å. Solvent accessible surface area (SASA) was measured using the surf tool of cpptraj, with the solvent shielding per probe determined as $1\text{-}(SASA_{measured}/SASA_{max})$, where $SASA_{max}$ is the SASA of the free probe (Fig. S1). For each TBA–thrombin complex, hierarchical agglomerative clustering was performed with respect to the RMSD of TBA nucleotides G2–T4 and G11–G14, and thrombin residues Lys33–Phe34, Asp63–Ile68, Arg75–Arg77A, and Glu80–Met84. In the case of the unbound aptamer, clustering was done with respect to nucleotides 2–4 and 11–14, which are primarily responsible for thrombin binding. Overlays of MD snapshots were generated by extracting every 3600th frame across all replicas for each system (50 frames total).

D-ABMD simulation protocol

Models for D-ABMD were generated from representative structures obtained across the 9×1 μs final MD production simulation dataset for each probe (Fig. S4A), using the RMSD of the binding interface (defined above) according to the hierarchical agglomerative algorithm. Representative structures were stripped of solvent and ions (except for the central K^+ of TBA), and re-solvated using a minimum distance of 12 Å from the box edge and re-ionized (Table S4). Minimization, heating, and equilibration steps were performed as described above. A center-of-mass (COM) type collective variable (CV) was defined as the distance between the potassium ion (K^+) coordinated to TBA and the COM of all atoms of Ile276(CG2), Gly259(N), and Thr92(CA), which are the most central residues of thrombin. 12 replicates of 50 ns simulations were run per system. A maximum force of 25.0 kJ mol^{-1} $Å^{-1}$ was applied when the coordination distance between each O6 oxygen in the GQ and K^+ exceeded 3.2 Å, which maintained $(G)O6\cdots K^+$ equilibrium coordination distances ($\sim$2.8 Å, Fig. S5). The structural integrity of thrombin and the aptamer was visually monitored throughout the D-ABMD process. The CV was driven from the bound distance of 28 Å to a maximum unbound distance of 60 Å using the SPLINE path mode, a resolution of 0.5 Å, a single harmonic, and a harmonic (unitless) value of 10. To monitor the application of the D-ABMD bias, energy was written to disk along with a restart file every 5 ps. Well-tempered dynamics were enabled with an artificial temperature of 5000 K. The driving bias was re-calculated every 100 ps. Bias potentials were converted to binding free energies using the nfe-umbrella-slice utility of Amber22. Data was extracted until the TBA ligand fully dissociated from thrombin, which occurred at COV $\approx$ 34 Å in all cases. All 12 free energy curves per probe were averaged and standard deviations calculated at each 0.07 Å step.

Quantum mechanical calculations

All DFT and TD-DFT calculations were performed with Gaussian 16 (revision C.01).[40] The ground state geometries were optimized using the ωB97X-D functional[49] with the double-ζ def2-SVP basis set.[50] For each probe, a conformational search was conducted about rotatable bonds, and the geometry with the lowest energy was selected. Solvent effects (solvent = water) were included in all geometry optimizations using the polarized continuum model (IEF-PCM) of Tomasi and coworkers.[51] Excited state geometries were optimized at the TD-ωB97X-D/def2-SVP level of theory using the linear response (LR-PCM) formalism. Single-point energy calculations were carried out at the TD-CAM-B3LYP/def2-SVP level of theory[52] using the corrected linear response (cLR-SMD) formalism.[53,54] This approach has proven to reliably describe TICT,[55] and yields profiles for the molecules considered in the present work in qualitative agreement with previous ADC(2) on protonated AnBtz and XMS-CASPT2 studies on comparable donor–acceptor dyes.[56,57] Relaxed geometric scans were performed over all rotatable bonds between the donor and acceptor moieties, with the exception of those associated with exocyclic methyl groups. Harmonic vibrational frequency calculations were conducted to confirm all stationary points correspond to local minima (*i.e.*, all local minima have only real/positive frequencies). Cartesian coordinates for all optimized geometries (.xyz) are available as SI.

Experimental methodolgy

All reagents and solvents were purchased from commercial suppliers and used as received. All solvents were dried over 4 Å molecular sieves. Ultraviolet-visible (UV-vis) spectra were obtained on a Cary 300-Bio UV-vis spectrophotometer equipped with a 6×6 multicell block Peltier temperature control unit. Fluorescence measurements were acquired on a Cary Eclipse fluorescence spectrophotometer. A stock solution of AnBtz was prepared as a 10 mM stock solution in DMSO, from which 1 μL was added to 499 μL of solvent to give a concentration of 20 μM for analysis.

The synthesis of AnBtz, (2-(4-dimethylaniline)benzothiazole), was carried out following known procedures.[58] 4-(Dimethylamino)benzaldehyde (202.6 mg, 1.34 mmol) and 2-aminothiophenol (187.0 mg, 1.47 mmol) were combined in 15 mL of EtOH and heated to reflux for 18 h. The reaction mixture was subsequently cooled to 0 °C and filtered to obtain the product as yellow crystals (286.7 mg, 1.12 mmol, yield = 83%). The product was characterized by ^{1}H NMR and ^{13}C NMR and was in agreement with the literature.[58]

Open Access Article. Published on 01 2568. Downloaded on 1/6/2569 14:33:01.
This article is licensed under a Creative Commons Attribution 3.0 Unported Licence.

Results and discussion

Classical MD simulations coupled with D-ABMD identify key differences in probe binding that rationalize the observed differential thrombin binding affinities

The three probes under investigation exhibit differential binding affinities to thrombin, with the measured dissociation constant being 23.7 nM for canonical TBA,[59] 15 ± 3 nM for AnBtz, 66 ± 5 nM for AnMeBtz, and 444 ± 19 nM for AnMeInd.[8] To uncover the underlying factors contributing to these binding differences, classical MD simulations were used to examine changes in the canonical TBA–thrombin binding face upon probe incorporation at the T3 position, while D-ABMD simulations were used to predict relative binding strengths. Although PDB ID: 4DII[60] is the most widely studied crystal structure of the canonical TBA–thrombin complex, MD simulations initiated from this binding configuration showed that all probes were highly dynamic across the simulations (Fig. S6A). As a result, despite contacts between the probe-decorated TBA and thrombin being periodically formed, these interactions come at the expense of those known to be important for canonical TBA–thrombin binding. For example, the probe disrupts interactions between Arg75 or Arg77A of thrombin and T4, G5, T13, or G14 of canonical TBA. This is perhaps not surprising since overlays of each probe at T3 in PDB ID: 4DII with respect to key backbone atoms (O3′ and O5′) results in several steric clashes (Fig. S7A). In fact, during classical MD simulations, thrombin unbinds from the modified TBA regardless of the probe considered (Fig. S6C), which does not correlate with the observed increased binding affinity upon incorporation of AnBtz at T3.[8]

A second canonical TBA–thrombin binding orientation has been identified using cytolysin A (ClyA) biological nanopores,[61] which was attributed to the configuration observed in the PDB ID: 1HAO[62] crystal structure that differs from 4DII by a 180° rotation about the TBA central axis prior to thrombin binding (Fig. S2). Furthermore, the same alternate binding configuration occurs when TBA is bound at thrombin exosite I and the larger HD22 aptamer is simultaneously bound at exosite II (PDB IDs: 5EW1 and 5EW2).[26] There is also evidence that the preferred TBA–thrombin binding configuration is impacted by modification of the TT loops.[14,23,61] For example, an abasic site (tetrahydrofuran) at T3 or T12 enhances the K_d of a particular pose,[61] with an abasic site at T3 inducing binding as per 1HAO (PDB ID: 4LZ4) and an abasic site at T12 resulting in binding as per 4DII (PDB ID: 4LZ1).[22] Furthermore, X-ray crystal structures of TBA containing lactose, glucose, or leucine bound *via* a triazole moiety to N3 of T3 (PDB IDs: 6Z8V, 6Z8W, and 6Z8X)[23] show the modified nucleotides bound in a thrombin hydrophobic pocket similar to that encapsulating T3 in PDB ID: 1HAO.[62] Previous computational studies have also revealed that bulky modifications at T3 prefer the 1HAO binding orientation.[14] Therefore, the 1HAO TBA–thrombin binding configuration was also considered for TBA containing the hemicyanine probes, with the complexes remaining well bound and stable throughout the simulations (Fig. S8–S10).

When canonical TBA is bound to thrombin according to the 1HAO binding pose (Fig. 2), T3 and T12 form many noncovalent interactions with thrombin over the course of the classical MD simulations (Fig. S11). Specifically, T3 π–π stacks with Tyr76 (47 ± 25% occupancy) and T12 is positioned in a hydrophobic pocket comprised of Ile24, Tyr117, His71, and Ile79. On the other hand, Tyr76 hydrogen bonds with O4′ in the T4 sugar moiety (67 ± 27%), and the T4 and T13 nucleobases stack against the GQ of TBA, which permits hydrogen bonding to each other as well as Arg75 and Arg77A. At the same time Arg75 stacks with G5 (83 ± 13%), while Arg77A stacks with G14 (38 ± 17%). Visual inspection of the D-ABMD simulation trajectories reveal that TBA disengagement from thrombin initially occurs in the region near T12, which is followed by disruption of Arg75 hydrogen bonds with T4, T13, and G5. To preserve the remaining strong contacts with thrombin, the TBA TT loops distort to contract around Tyr76 and Arg77A, while exosite I distorts to maintain hydrogen bonding between Tyr76 and T4. The hydrogen bonds between T4 and T13 and Arg77A are the last TBA–thrombin contacts to be severed as the complex dissociates, highlighting the importance of these interactions for the high affinity of TBA to thrombin. Overall, unbinding of canonical TBA from thrombin requires maximum work of −3.9 ± 0.3 kcal mol^{-1} (Fig. 3A).

The AnMeInd probe is highly dynamic at the T3 position of the TBA when bound to thrombin (Fig. S8–S10), with overlays of classical MD snapshots highlighting that the probe primarily rests against the thrombin surface (Fig. 4A-i). Indeed, the steric

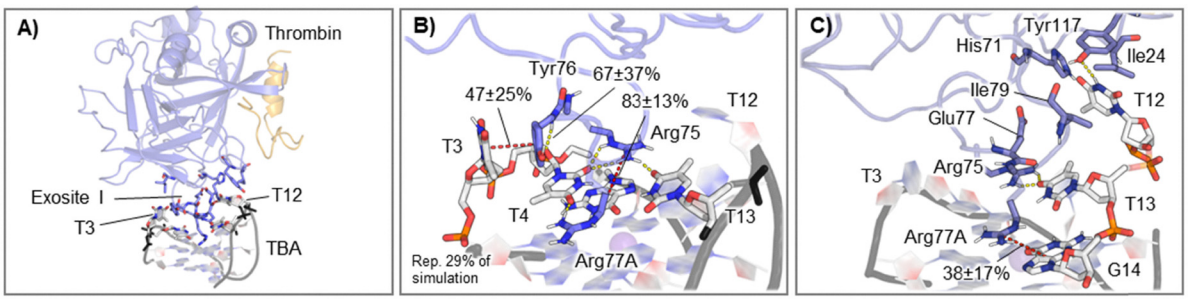

Fig. 2 (A) Canonical TBA–thrombin complex bound according to PDB ID: 1HAO. TBA–thrombin binding interface around (B) T3 and T4, and (C) T12, T13, and G14. Stacking interactions shown with red dotted lines and hydrogen-bonding interactions with yellow dotted lines. Select average occupancies and standard deviations across replicates are provided.

 This journal is © the Owner Societies 2025

Open Access Article. Published on 01 2568. Downloaded on 1/6/2569 14:33:01.
This article is licensed under a Creative Commons Attribution 3.0 Unported Licence.

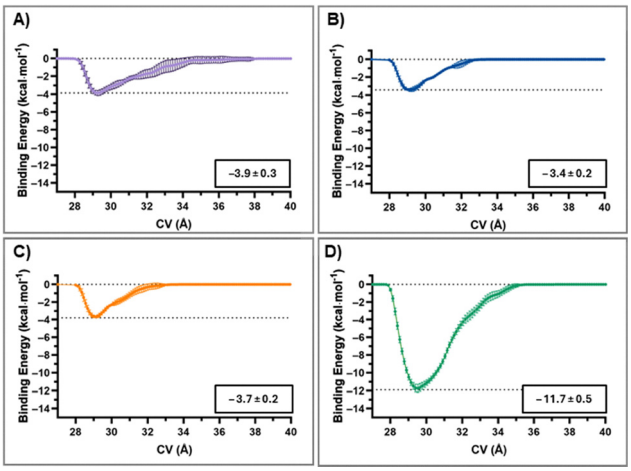

Fig. 3 D-ABMD average (with standard deviation) binding free energy curves determined over 12 replicate simulations for (A) canonical T, (B) AnMeInd, (C) AnMeBtz, and (D) AnBtz at T3 of TBA to thrombin. The boxes in each graph indicate the average and standard deviation point of maximum work.

repulsion between the exocylic methyl groups on the cationic AnMeInd acceptor ring and Arg73 coupled with electrostatic repulsion between the positively charged probe and Arg67, Lys70, and Arg75 likely prevent probe insertion deep into the thrombin pocket (Fig. 4B-i). At the thrombin surface, the representative structure from the dominant conformation reveals the edge of the indolinium ring forming a T-shaped interaction with the face of Phe34 (32 ± 13% occupancy), the backbone of Gln38 directed toward the charged ring (7 ± 4%), and the acceptor moiety π–π stacking with Arg67 (45 ± 24%). The donor ring of the probe stacks with Tyr76 (62 ± 18%). Tyr76 and Arg75 hydrogen bond with the neighboring T4 of TBA (Fig. S12), albeit with reduced occupancy relative to canonical TBA (Fig. S11). In the representative structures from other (minor) clusters, slight distortions from this dominant conformation occur that primarily shift the G14–G15 edge of TBA closer to the thrombin center of mass, movement that correlates with the probe detachment from the protein periodically seen as part of the system dynamics (Fig. 4A-i). Indeed, D-ABMD simulations suggest that minimal work (−3.4 ± 0.2 kcal mol^{-1}, Fig. 3B) is required to break the Tyr76 and Arg75 hydrogen bonds with T4 in conjunction with detachment of AnMeInd from the thrombin surface, while maintaining the global fold of canonical TBA, which correlates with the measured decreased thrombin binding affinity upon probe incorporation into TBA.[8]

As discussed for AnMeInd, the positively-charged AnMeBtz likely experiences electrostatic repulsion with Arg67, Lys70, and Arg75, which prevents insertion of the probe deep into the thrombin pocket. As a result, AnMeBtz similarly rests against the edge of thrombin, although exhibits increased dynamics (Fig. 4B-ii and Fig. S8–S10, S13). In the dominant conformation, the acceptor ring forms π–π stacking interactions with Phe34 (6 ± 21%) and Arg67 (18 ± 33%) as well as edge-on interactions with Met32 (12 ± 24%) and Gln38 (10 ± 11%, Fig. 4B-ii). The donor moiety does not form long-lasting interactions with thrombin. Nevertheless, during D-ABMD simulations, the TT loops visibly resist dissociation, with the loops stretching to maintain interactions with thrombin as TBA disengages. Specifically, a T12 (N3···O) Ile61 hydrogen bond is maintained, which outlasts the interactions between Arg77A or Arg75 and TBA. Unlike the rapid unbinding of AnMeInd from the thrombin surface during D-AMBD, AnMeBtz slides along the face of thrombin, forming interactions with Phe34, Met32, Lys80, Gln39, Tyr76, and Arg75 before unbinding from the protein. This drawn-out disengagement process results in a greater mean of the maximum work for AnMeBtz (−3.7 ± 0.2 kcal mol^{-1}, Fig. 3C) compared to AnMeInd (−3.4 ± 0.2 kcal mol^{-1}, Fig. 3B), but less than canonical TBA (−3.9 ± 0.3 kcal mol^{-1}, Fig. 3A), rationalizing the relative experimental binding affinities.[8]

Unlike the probes with the olefin linker, classical MD simulations demonstrate that AnBtz can deeply intercalate into a thrombin pocket located above Tyr76, which is formed by Arg67, Phe34, Leu65, Gln38, and Met32 (Fig. 4A-iii and B-iii). This binding configuration is well maintained across all replica simulations, with slightly different relative arrangements of thrombin and TBA throughout the simulations highlighting the dynamic nature of the complex (Fig. S8–S10 and S14). Nevertheless, AnBtz is much less dynamic in this pocket than the other probes, which bind to the surface of thrombin. Indeed, the acceptor ring of AnBtz forms persistent π–π interactions with both Phe34 (69 ± 39%) and Arg67 (64 ± 12%), while also exhibiting a consistent edge-on interaction with Met32 (85 ± 37%). Although the donor ring of AnBtz does not π–π stack with Tyr76 (occupancy < 1%), and the hydrogen bond between Tyr76 and T4 is significantly weakened (36 ± 30%) compared to canonical TBA (67 ± 37%), no other canonical TBA–thrombin interactions are significantly altered by the presence of AnBtz at T3 (Fig. S11 and S14). The persistent intercalation of the probe into the thrombin pocket contributes to the enhanced thrombin binding affinity of AnBtz–TBA compared to canonical TBA, with D-ABMD revealing −11.7 ± 0.5 kcal mol^{-1} is required to disengage the modified TBA from the target (Fig. 3D). Along the disengagement pathway, AnBtz π–π stacking interactions with Phe34 and Arg67 are the last to breakdown, being persistent even after the hydrogen bonds with Arg75, Tyr76, and Arg77A are disrupted. This correlates with the reported enhanced thrombin binding affinity upon incorporation of AnBtz into TBA.[8]

Overall, classical MD combined with D-ABMD simulations provide structural rationalization for the observed differential binding affinities upon probe incorporation at T3 of TBA. Indeed, the qualitative trend of decreasing binding affinity seen experimentally, namely AnBtz > TBA > AnInd > AnMeBtz, is reproduced by the D-ABMD simulations. Furthermore, classical MD simulations uncover key differences in probe binding that explain this trend. Specifically, our simulations indicate that a deep hydrophobic pocket that can bind the probes exists above Tyr76, which is formed by Arg67, Lys70, and Lys14A. As this pocket is rich in both aromatic and charged residues, non-decorated, planar, and neutral probes (*e.g.*, AnBtz) are better

Open Access Article. Published on 01 2568. Downloaded on 1/6/2569 14:33:01.
This article is licensed under a Creative Commons Attribution 3.0 Unported Licence.

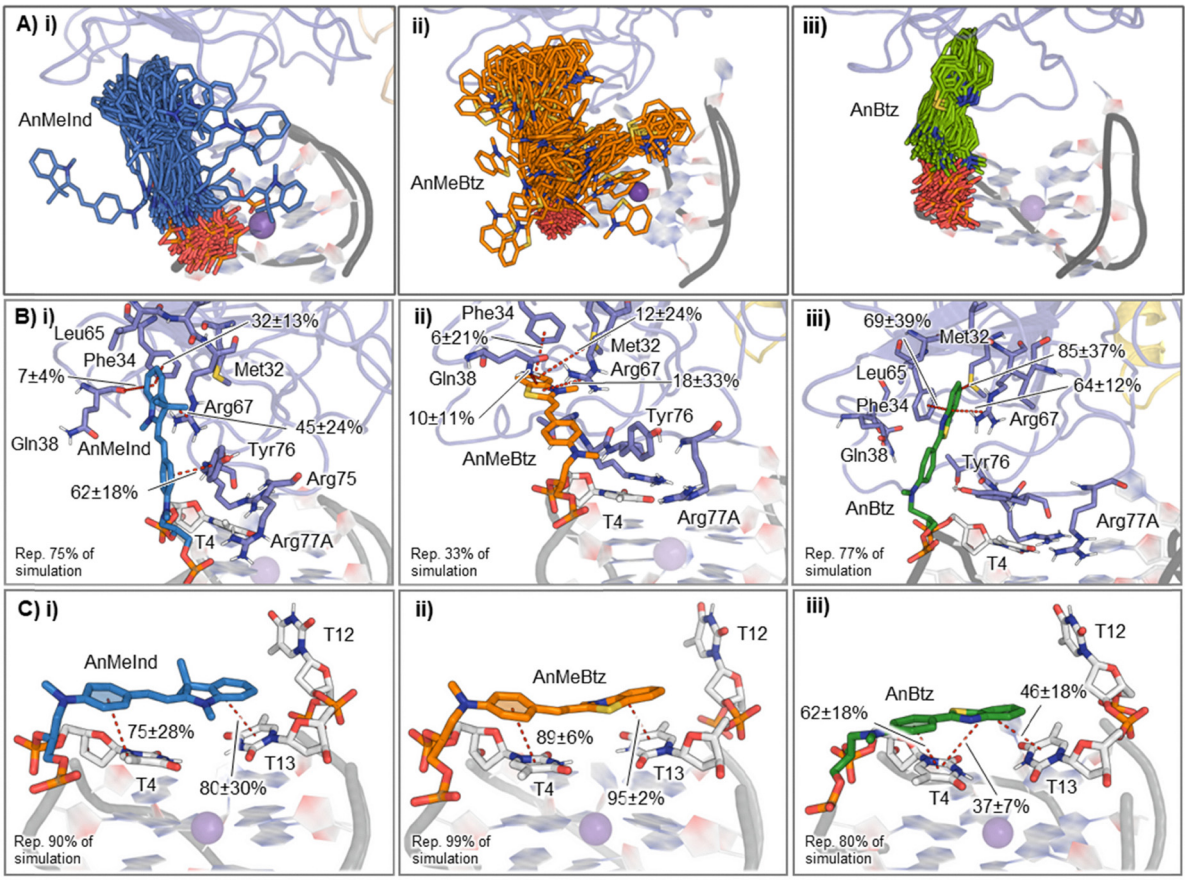

Fig. 4 (A) 100 frame overlays of the T3 probe across all MD replicates initiated from PDB ID: 1HAO. Representative structures of (B) thrombin bound and (C) unbound TBA containing (i) AnMeInd, (ii) AnMeBtz, and (iii) AnBtz at T3. π–π interactions shown as red dotted lines.

accommodated. In contrast, electrostatic repulsion from Arg67 and Lys70, as well as Arg75, prevents cationic probes (*e.g.*, AnMeBtz and AnMeInd) from binding. Out-of-plane exocyclic substituents (*e.g.*, methyl groups in AnMeInd) further generate steric interactions with Arg67 that prevent efficient intercalation. Furthermore, the olefin bridge of both AnMeInd and AnMeBtz is longer than the C–C linker of AnBtz (by ∼2.2 Å), which further hinders effective intercalation into the thrombin pocket. Indeed, overlays of each probe onto the T3 position according to key (O3′ and O5′) backbone atoms illustrates that the probes containing the olefin bridge do not fit in this pocket (Fig. S7B). Thus, our MD simulations have identified key chemical features for optimal probe design in terms of the charge of the acceptor moiety and the linker length.

While TD-DFT suggests the cationic probes have similar propensities for TICT formation, MD simulations highlight differences in probe microenvironment upon thrombin binding that yield differential fluorescence responses

With the relative binding affinities for thrombin rationalized for the three probes, we turn our attention to differences in the photophysical responses, which decrease as AnBtz = AnMeInd (I_{rel} = 4.0) > AnMeBtz (I_{rel} = 2.0).[8] Initially, TD-DFT calculations were used to understand the propensity of the cationic probes to undergo TICT (Fig. 5), based on previous successes of such calculations to rationalize the structure–activity relationship of TICT-based fluorophores[63–67] and our own methodology validation (Fig. S15). Specifically, the lowest singlet (S_1) electronic energy profile (EEP) was utilized to analyze the rotational behavior of the donor/linker fragment, with a small rotational energy barrier (E_{RB}) and a large, negative driving energy (E_{DE}) from the locally excited or ICT state to the TICT state strongly favoring TICT.[12,55,68]

TD-DFT calculations show that both AnMeInd and AnMeBtz undergo a HOMO → LUMO transition with a strong oscillator strength, indicating efficient electronic excitation (Fig. 5A). Although the frontier molecular orbitals are uniformly distributed in both probes, the S_0 HOMO is slightly more localized on the donor moiety, while the S_0 LUMO exhibits a stronger localization on the acceptor moiety. Examination of the S_1 EEP suggests that rotation about the amine donor does not substantially contribute to TICT as E_{DE} is endergonic for both probes. Instead, consideration of rotation about each bond in the linker reveals the two cationic probes likely undergo TICT formation upon 90° rotation about the olefin bond, which results in a lower barrier and exergonic process (Fig. 5C-i and ii). Indeed, rotation with respect to other bonds along the flexible π-bridge likely do not significantly contribute to TICT

 This journal is © the Owner Societies 2025

Open Access Article. Published on 01 2568. Downloaded on 1/6/2569 14:33:01.
This article is licensed under a Creative Commons Attribution 3.0 Unported Licence.

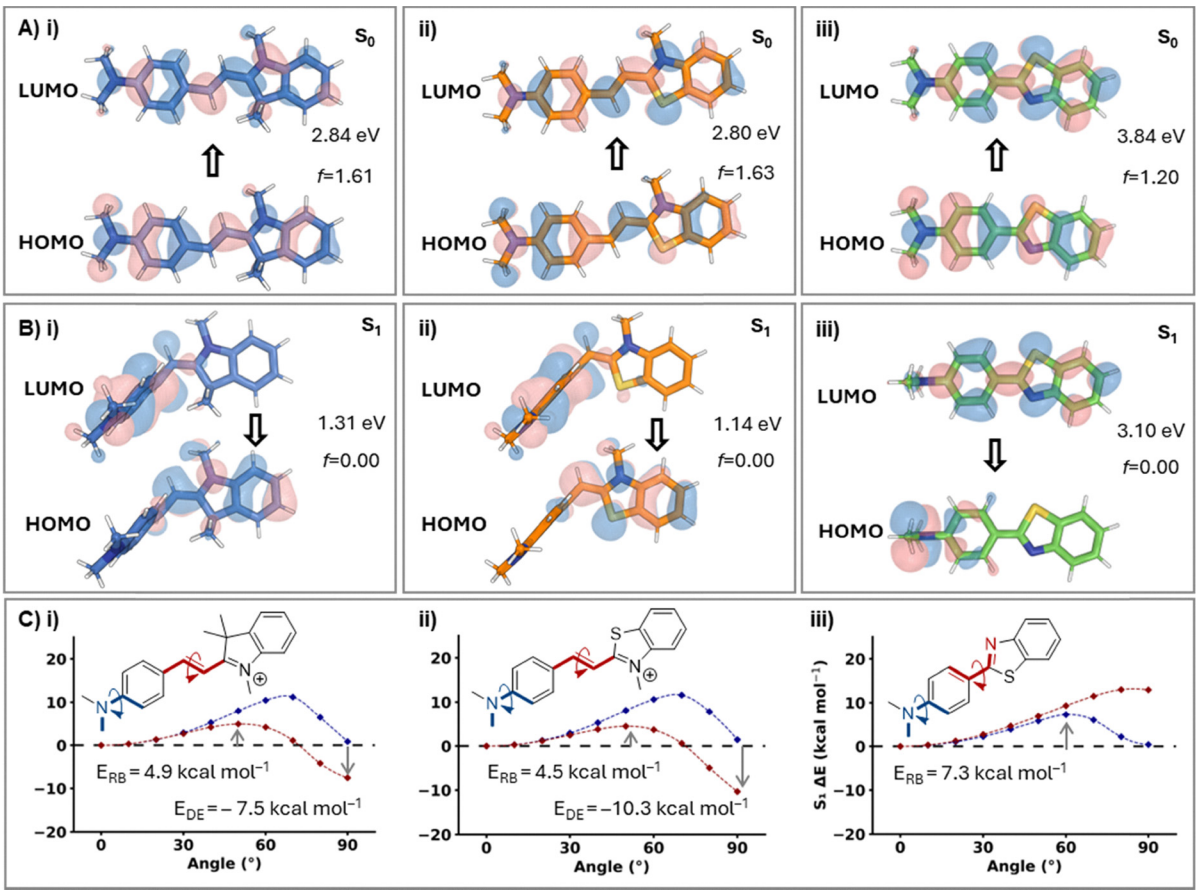

Fig. 5 (A) PCM-ωB97X-D/def2-SVP (water) S_0 molecular geometries with HOMO and LUMO isosurfaces. The oscillator strength (*f*) and vertical energy of the HOMO → LUMO transition is provided. (B) TD-PCM-ωB97X-D/def2-SVP (water) S_1 molecular geometries frozen at 90°, with HOMO, and LUMO isosurfaces. (C) TD-cLR-SMD-CAM-B3LYP/def2-SVP//PCM-ωB97X-D/def2-SVP (water) S_1 TICT EEP for (i) AnMeInd, (ii) AnMeBtz, and (iii) AnBtz. The color of the trace corresponds to the scanned dihedral angle.

due to a higher E_{RB} and less favorable E_{DE} (Fig. S16). In fact, the low oscillator strength of the twisted conformation following 90° olefin rotation supports the nonemissive nature of this state (Fig. 5B). Nevertheless, the E_{RB} for twisting about the olefin bond is comparable for AnMeInd and AnMeBtz (4.9 and 4.5 kcal mol^{-1}, respectively). Furthermore, both probes possess a sufficient E_{DE} for TICT state formation (−7.5 and −10.3 kcal mol^{-1}, respectively; Fig. 5C-i and ii). This indicates that the inherent propensity for AnMeInd and AnMeBtz to undergo TICT is unlikely to be the primary factor behind the observed differences in the fluorescence responses upon probe-decorated TBA binding to thrombin.

To evaluate the impact of changes in the local microenvironment of the probe upon binding to thrombin on the observed fluorescence enhancement, classical MD simulations were considered for both the unbound probe–TBA complexes and the corresponding thrombin-bound forms. The unbound aptamer containing AnMeBtz or AnMeInd remained highly stable over the simulations and exhibited similar dynamics in each nucleotide (Fig. S17 and S18). Both probes are consistently aligned with respect to T4 and T13 in unbound TBA (representative structure >90% occupancy, Fig. 4C). Both probes exhibit comparable levels of solvent exposure in this state, ranging from 48–50% (Fig. 6A). However, subtle differences in stacking interactions were observed, with AnMeInd exhibiting stacking occupancies of 75 ± 28% with T4 and 80 ± 30% with T13, whereas AnMeBtz showed stronger interactions (89 ± 6% and 95 ± 2% occupancy, respectively; Fig. 4C-i, ii and Fig. S17 and S18). Indeed, AnMeInd is more conformationally flexible in the unbound TBA state.

Upon thrombin binding, AnMeInd undergoes a greater increase in solvent shielding compared to AnMeBtz (10.8% *vs.* 9.6%, Fig. 6A). Indeed, as previously discussed, AnMeBtz exhibits greater fluctuations than AnMeInd in the TBA–thrombin complex over the course of the classical MD simulations (Fig. 4A and Fig. S8–S10), which permits AnMeBtz to explore more diverse and solvent exposed conformations when bound to thrombin. As a result, the nonemissive TICT state, which is typically favored in polar environments, is more prominent for AnMeBtz, at least in part leading to the observed reduced fluorescent response (I_{rel} = 2.0 *vs.* 4.0). In contrast, the nonemissive TICT state is suppressed for AnMeInd, which results in fluorescence recovery and prolonged excited-state lifetimes, rationalizing the observed fluorescent enhancement.[69] Notably, both AnMeInd and AnMeBtz exhibit similar conformational rigidity upon thrombin binding (173.5 ± 33.4° *vs.* 189.5 ± 33.5°, Fig. 6C), with minimal change between the unbound and

Open Access Article. Published on 01 2568. Downloaded on 1/6/2569 14:33:01.
This article is licensed under a Creative Commons Attribution 3.0 Unported Licence.

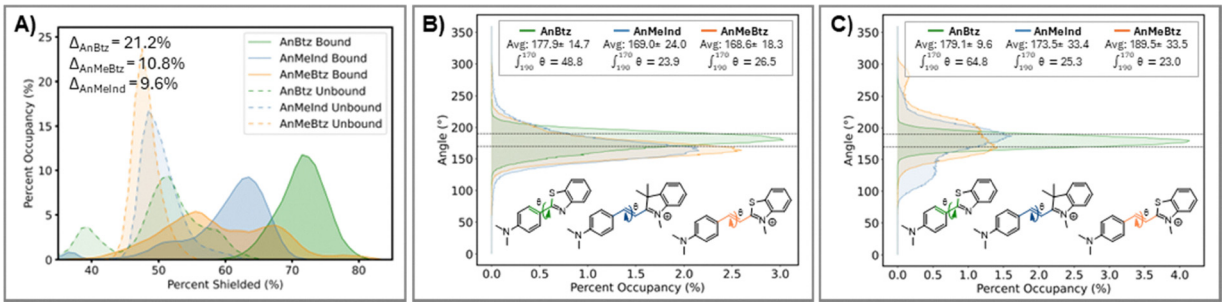

Fig. 6 (A) Histograms of the degree of solvent shielding of the probes in the unbound (dotted trace) and thrombin bound (solid trace) states across MD simulation replicas. Histograms of the TICT-active dihedral angles for (B) unbound and (C) thrombin bound modified TBA across MD simulation replicas.

bound states (Fig. 6B). This suggests that both probes experience comparable structural constraints in the thrombin-bound complex.

Given that both cationic probes share a comparable intrinsic propensity for TICT and exhibit similar structural dynamics in both unbound and thrombin-bound states, these factors are unlikely to be the primary drivers of the observed differences in fluorescence response. Rather, the reduced fluorescence response of AnMeBtz likely stems from its increased solvent exposure in the thrombin-bound state, which facilitates TICT. Moreover, the exocyclic methyl groups of AnMeInd likely prevent optimal contact with T4/T13 in the unbound aptamer, promoting partial probe disengagement, which increases rotational freedom upon excitation and contributes to lower background fluorescence, thereby amplifying the observed fluorescence enhancement upon thrombin binding. Thus, although careful design is required to preserve target binding affinity, intentionally preventing stable, noncovalent interactions in the unbound aptamer state using exocyclic substituents offers a viable strategy to reduce background fluorescence by enabling TICT without the need to first overcome stabilizing contacts with the aptamer scaffold.

Distinct from the cationic probes, combined classical MD simulations, TD-DFT calculations, and experimental fluorescent studies suggest neutral AnBtz acts as a photobase

Similar to the cationic probes, classical MD simulations reveal that AnBtz at the T3 position lays flat across the T4 and T13 nucleotides of unbound TBA (Fig. 4C-iii). Persistent π–π stacking is observed with T4 through both the donor (62 ± 18%) and acceptor (37 ± 7%) moieties, along with additional stacking between the acceptor ring and T13 (46 ± 18%). As a result, the probe demonstrates high structural rigidity (Fig. S19 and Table S5), with biaryl coplanarity (10.2 ± 5.5°, avg. linker dihedral angle = 177.9 ± 14.7°). Notably, this rigid and planar conformation is maintained upon thrombin binding (Fig. 4A, 6C, and Fig. S19). However, AnBtz exhibits significantly greater solvent shielding upon thrombin binding (21.2%) than AnMeInd (9.6%). This shielding would enhance fluorescence for AnBtz, which contrasts the similar fluorescence responses for AnBtz and AnMeInd (I_{rel} = 4.0).[8] To investigate this discrepancy, we examined the excited-state behavior of AnBtz (Fig. 5C-iii and Fig. S15). Unlike the cationic probes, rotation of the benzothioazole moiety about the C–C linker on the S_1 surface is predicted to be endergonic, which was previously reported for the benzimidazole analogue.[67] Furthermore, TD-DFT predicts a E_{RB} of 7.3 kcal mol^{-1} and a near thermoneutral E_{DE} of 0.4 kcal mol^{-1} for rotation about the amine donor. Thus, the S_1 EEP suggests that the neutral probe likely does not undergo TICT state formation upon photoexcitation. This finding is consistent with experimental viscosity tests, where AnBtz exhibited poor FMR character when transitioning from MeOH to MeOH:glycerol mixtures (Fig. 7A and Table S6).[8]

Classical MD simulations and TD-DFT results suggest that another microenvironmental factor must be responsible for the fluorescence response of AnBtz. Indeed, the simulations highlight that the neutral probe experiences the greatest increase in solvent shielding upon thrombin binding (21.2%, Fig. 6A), indicating a distinct environmental shift compared to the cationic probes. One plausible explanation for the differential fluorescence modulation is that AnBtz functions as a photobase – a molecule that exhibits higher proton affinity in the excited state than in the ground state. A photobase can result from a change in electronic structure upon photoexcitation, which allows the excited molecule to abstract a proton from the environment. Several experimental and computational investigations by the Dawlaty and Petit laboratories have showcased the photobasicity of nitrogen-containing heteroaromatic ring systems, with K_B values increasing by up to 10 orders of magnitude upon photoexcitation.[70–75]

TD-DFT calculations suggest that the nitrogen of the benzothiozole moiety becomes more electron rich upon photoexcitation of AnBtz (Fig. 7B). Compared to the neutral species (Fig. 5C-iii), AnBtz-H likely exhibits TICT state formation upon rotation of both the C–N of the donor (E_{RB} = 5.3, E_{DE} = −7.9 kcal mol^{-1}) and the C–C biaryl bridge (E_{RB} = 2.0, E_{DE} = −5.9 kcal mol^{-1}, Fig. 7C). Protonation to yield AnBtz-H creates a stronger acceptor moiety, which promotes TICT. To experimentally validate the feasibility of proton abstraction by AnBtz, we measured the fluorescence intensity of AnBtz in various nonpolar, polar-protic, and polar-aprotic solvents. We found the fluorescence intensity was similar irrespective of the dielectric constant; however, there was a dramatic drop in intensity in trifluoroethanol (TFE to EtOH, I_{rel} = 4.00, Fig. 7D and Table S6). To establish a relationship between the pK_a of the solvent and viscosity, we measured the fluorescence intensity change from

 This journal is © the Owner Societies 2025

Open Access Article. Published on 01 2568. Downloaded on 1/6/2569 14:33:01.
This article is licensed under a Creative Commons Attribution 3.0 Unported Licence.

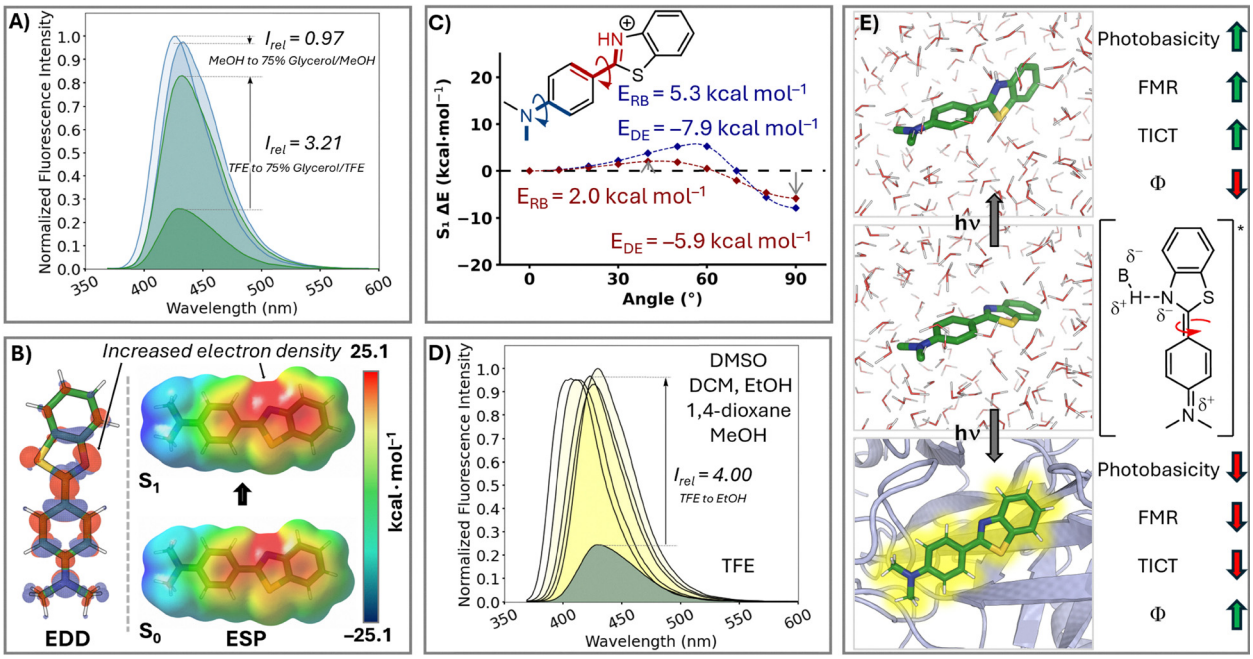

Fig. 7 (A) Emission spectra of AnBtz, highlighting response to viscosity. (B) Calculated electron density difference isosurface. The blue and red lobes represent regions of decrease and increase of electronic density upon excitation. Calculated electrostatic potential map of S_0 and S_1 of AnBtz. (C) TD-cLR-SMD-CAM-B3LYP/def2-SVP//PCM-ωB97X-D/def2-SVP (water) S_1 TICT EEP for AnBtz-H. The color of the trace corresponds to the scanned dihedral angle. (D) Emission spectra of AnBtz in different solvents. (E) Illustrated summary of environmental effects on the fluorescence of AnBtz.

TFE to a 25% TFE:glycerol mixture. While MeOH to MeOH:glycerol led to a mild decrease in intensity upon increased viscosity (I_{rel} = 0.97), TFE to TFE:glycerol led to substantial increase in intensity (I_{rel} = 3.21), supporting FMR characteristics (Fig. 7A). Therefore, the AnBtz probe appears to act as a photobase, with excited-state protonation likely driving the observed turn-on response.

Overall, we proposed that upon photoexcitation in an acidic enough environment, such as the 10 mM Tris-HCl buffer at pH 7.3 used experimentally,[8] a protonated AnBtz-H species is generated, which functions as an FMR and will efficiently undergo TICT. Thus, AnBtz in unbound TBA is likely protonated through solvent exposure and does not exhibit significant fluorescence, consistent with the low background signal observed experimentally for the free AnBtz probe (this work) and when positioned at T3 of TBA.[8] However, when intercalated within the hydrophobic pocket of thrombin, the probe is significantly shielded from solvent (Fig. 6A), which prevents protonation and permits strong fluorescence (Fig. 7E). This interplay between the local environment photoinduced protonation and TICT offers a mechanistic explanation for the fluorescence enhancement observed for AnBtz (I_{rel} = 4.0),[8] and points to a new important design principle that can direct development of improved probes.

Conclusion

By employing a range of computational (MD, D-ABMD, TD-DFT) and experimental approaches, we have provided critical insights into the differential binding affinity and PIFE for a family of cyclic *N*-glycol-linked 4-formyl-aniline probes. In terms of binding affinity, classical MD coupled with D-ABMD simulations highlight that the neutral AnBtz probe is well accommodated in a hydrophobic pocket of thrombin that is rich in aromatic and charged residues, resulting in the strongest binding affinity for the protein target. In contrast, cationic AnMeInd and AnMeBtz exhibit electrostatic repulsion with charged residues in the binding pocket that prevent efficient intercalation and reduce binding affinity, with exocyclic methyl groups of AnMeInd generating further steric interactions.

While TD-DFT calculations suggest similar propensities for TICT formation among the cationic probes, MD simulations reveal differences in probe microenvironments upon thrombin binding. Indeed, the methyl substituents of AnMeInd reduce probe contacts with the aptamer scaffold, which enhances TICT in the unbound state compared to AnMeBtz. In direct complement, the additional substituents adjust probe binding location in the thrombin hydrophobic pocket, which increases solvent shielding, probe rigidity, and TICT suppression upon target binding, rationalizing the observed enhanced fluorescence response for AnMeInd compared to AnMeBtz.

Distinct from the cationic probes, combined classical MD, TD-DFT, and experimental fluorescence studies suggest that the neutral AnBtz probe with the most promise operates *via* a different mechanism involving excited-state proton transfer. Specifically, AnBtz behaves as a photobase, which undergoes protonation upon excitation in aqueous solution. In the unbound aptamer, the solvent exposed AnBtz is susceptible to excited state protonation and subsequent TICT, which induces

Open Access Article. Published on 01 2568. Downloaded on 1/6/2569 14:33:01.
This article is licensed under a Creative Commons Attribution 3.0 Unported Licence.

rapid decay through nonradiative pathways that results in fluorescence quenching. However, when the probe is intercalated into thrombin, the hydrophobic, solvent-shielded environment inhibits protonation, stabilizing an emissive neutral state and enabling fluorescence recovery.

Our findings highlight the importance of considering conformational rigidity, noncovalent interactions with the aptamer scaffold, and local environmental effects when designing fluorescent probes. To optimize fluorescence enhancement *via* PIFE, future probe designs should reduce background fluorescence by prioritizing TICT suppression through enhanced solvent shielding and increased rigidity upon target binding. Incorporating photobasicity offers another promising approach, allowing for a more pronounced TICT-based fluorescence turn-on response without the need for an intrinsically charged probe. These design principles establish a framework for the rational development of high-performance fluorescent probes, expanding their applicability in biosensing, nucleic acid biotechnology, and other fluorescence-based detection platforms.

Author contributions

M. T. M. was involved in conceptualization, data curation, formal analysis, investigation, methodology, project administration, software, validation, and visualization. A. P. was involved in conceptualization, data curation, formal analysis, investigation, methodology, and visualization. R. E. J. was involved in data curation. K. T. R. was involved in data curation. R. A. M. was involved in funding acquisition, methodology, project administration, resources, and supervision. S. D. W. was involved in conceptualization, formal analysis, funding acquisition, methodology, project administration, resources, and supervision. All authors contributed to writing – original draft preparation and writing – reviewing and editing.

Conflicts of interest

There are no conflicts to declare.

Data availability

Supplementary figures and data can be found in the SI. Molecular dynamics structures, set-up files, custom parameters, in-house stacking scripts as well as optimized (TD)-DFT structures (xyz) used in this publication may be found at: DOI: **https://doi.org/10.5281/zenodo.15428289**.

NMR characterization, photophysical properties, synthetic details, computational details and SI Figures/Tables. See DOI: **https://doi.org/10.1039/d5cp01851j**

Acknowledgements

This work was funded by the Natural Sciences and Engineering Research Council (NSERC) of Canada [2025-04391], the Canada Research Chair Program [2021-00484], and the University of Lethbridge to SDW and NSERC Discovery Grant [2025-04087] to RAM. MTM thanks NSERC, the RNA Innovation program (NSERC CREATE), and the University of Lethbridge for student scholarships. AP thanks the Alberta Innovates Postdoctoral Fellowships Program. SDW also thanks computational resources provided by the Digital Research Alliance of Canada (the Alliance).

References

1 S. C. Smith, Jr., A. Collins, R. Ferrari, D. R. Holmes, Jr., S. Logstrup, D. V. McGhie, J. Ralston, R. L. Sacco, H. Stam, K. Taubert, D. A. Wood and W. A. Zoghbi, *Circulation*, 2012, **126**, 2769–2775.
2 S. S. Mahmood, D. Levy, R. S. Vasan and T. J. Wang, *Lancet*, 2014, **383**, 999–1008.
3 H. Ten Cate and H. C. Hemker, *J. Am. Heart Assoc.*, 2016, **5**, e003553.
4 P. A. Kyrle and S. Eichinger, *Lancet*, 2005, **365**, 1163–1174.
5 B. Zoller, P. G. de Frutos, A. Hillarp and B. Dahlback, *Haematologica*, 1999, **84**, 59–70.
6 A. Singh-Manoux, M. J. Shipley, J. A. Bell, M. Canonico, A. Elbaz and M. Kivimaki, *CMAJ*, 2017, **189**, E384–E390.
7 B. Santosh and P. K. Yadava, *BioMed Res. Int.*, 2014, **2014**, 540451.
8 R. E. Johnson, M. T. Murray, L. J. Bycraft, P. Myler, S. D. Wetmore and R. A. Manderville, *Bioconjugate Chem.*, 2023, **34**, 2066–2076.
9 R. E. Johnson, M. T. Murray, L. J. Bycraft, S. D. Wetmore and R. A. Manderville, *Chem. Sci.*, 2023, **14**, 4832–4844.
10 R. E. Johnson, M. T. Murray, D. J. Roby, L. J. Bycraft, Z. R. Churcher, S. Yadav, P. E. Johnson, S. D. Wetmore and R. A. Manderville, *ACS Sens.*, 2023, **8**, 4756–4764.
11 J. Zhang, X. Chai, X. P. He, H. J. Kim, J. Yoon and H. Tian, *Chem. Soc. Rev.*, 2019, **48**, 683–722.
12 C. Wang, W. Chi, Q. Qiao, D. Tan, Z. Xu and X. Liu, *Chem. Soc. Rev.*, 2021, **50**, 12656–12678.
13 J. Maillard, K. Klehs, C. Rumble, E. Vauthey, M. Heilemann and A. Furstenberg, *Chem. Sci.*, 2020, **12**, 1352–1362.
14 M. T. Murray and S. D. Wetmore, *Nucleic Acids Res.*, 2024, **52**, 10823–10835.
15 K. L. Fadock, R. A. Manderville, P. Sharma and S. D. Wetmore, *Org. Biomol. Chem.*, 2016, **14**, 4409–4419.
16 D. J. M. Blanchard, K. L. Fadock, M. Sproviero, P. S. Deore, T. Z. Cservenyi, R. A. Manderville, P. Sharma and S. D. Wetmore, *J. Mater. Chem. C*, 2016, **4**, 2915–2924.
17 T. Z. Cservenyi, A. J. Van Riesen, F. D. Berger, A. Desoky and R. A. Manderville, *ACS Chem. Biol.*, 2016, **11**, 2576–2582.
18 C. Riccardi, E. Napolitano, C. Platella, D. Musumeci and D. Montesarchio, *Pharmacol. Ther.*, 2020, **217**, 107649.
19 L. C. Bock, L. C. Griffin, J. A. Latham, E. H. Vermaas and J. J. Toole, *Nature*, 1992, **355**, 564–566.
20 R. E. Johnson, A. J. Van Riesen and R. A. Manderville, *Bioconjugate Chem.*, 2021, **32**, 2224–2232.

Open Access Article. Published on 01 2568. Downloaded on 1/6/2569 14:33:01.
This article is licensed under a Creative Commons Attribution 3.0 Unported Licence.

21 R. Dolot, C. H. Lam, M. Sierant, Q. Zhao, F. W. Liu, B. Nawrot, M. Egli and X. B. Yang, *Nucleic Acids Res.*, 2018, **46**, 4819–4830.
22 A. Pica, I. Russo Krauss, A. Merlino, S. Nagatoishi, N. Sugimoto and F. Sica, *FEBS J.*, 2013, **280**, 6581–6588.
23 I. Smirnov, N. Kolganova, R. Troisi, F. Sica and E. Timofeev, *Mol. Ther.–Nucleic Acids*, 2021, **23**, 863–871.
24 R. Troisi, C. Riccardi, K. Perez de Carvasal, M. Smietana, F. Morvan, P. Del Vecchio, D. Montesarchio and F. Sica, *Mol. Ther.–Nucleic Acids*, 2022, **30**, 585–594.
25 I. Russo Krauss, A. Merlino, C. Giancola, A. Randazzo, L. Mazzarella and F. Sica, *Nucleic Acids Res.*, 2011, **39**, 7858–7867.
26 A. Pica, I. Russo Krauss, V. Parente, H. Tateishi-Karimata, S. Nagatoishi, K. Tsumoto, N. Sugimoto and F. Sica, *Nucleic Acids Res.*, 2016, **45**, 461–469.
27 P. Seelam Prabhakar, R. A. Manderville and S. D. Wetmore, *Molecules*, 2019, **24**, 2908.
28 A. J. Van Riesen, K. L. Fadock, P. S. Deore, A. Desoky, R. A. Manderville, S. Sowlati-Hashjin and S. D. Wetmore, *Org. Biomol. Chem.*, 2018, **16**, 3831–3840.
29 M. Sproviero, K. L. Fadock, A. A. Witham, R. A. Manderville, P. Sharma and S. D. Wetmore, *Chem. Sci.*, 2014, **5**, 788–796.
30 R. Galindo-Murillo, J. C. Robertson, M. Zgarbová, J. Šponer, M. Otyepka, P. Jurečka and T. E. Cheatham, 3rd, *J. Chem. Theory Comput.*, 2016, **12**, 4114–4127.
31 J. A. Maier, C. Martinez, K. Kasavajhala, L. Wickstrom, K. E. Hauser and C. Simmerling, *J. Chem. Theory Comput.*, 2015, **11**, 3696–3713.
32 H. W. Horn, W. C. Swope, J. W. Pitera, J. D. Madura, T. J. Dick, G. L. Hura and T. Head-Gordon, *J. Chem. Phys.*, 2004, **120**, 9665–9678.
33 T. Peng, T.-M. Chang, X. Sun, A. V. Nguyen and L. X. Dang, *J. Mol. Liq.*, 2012, **173**, 47–54.
34 R. Dennington, T. A. Keith and J. M. Millam, *GaussView 6.0.16*, 2016, vol. 16.
35 Open-source cheminformatics, **https://www.rdkit.org**.
36 A. K. Rappe, C. J. Casewit, K. S. Colwell, W. A. Goddard and W. M. Skiff, *J. Am. Chem. Soc.*, 1992, **114**, 10024–10035.
37 A. D. Becke, *J. Chem. Phys.*, 1993, **98**, 5648–5652.
38 S. Grimme, S. Ehrlich and L. Goerigk, *J. Comput. Chem.*, 2011, **32**, 1456–1465.
39 P. C. Hariharan and J. A. Pople, *Theor. Chim. Acta*, 1973, **28**, 213–222.
40 M. J. Frisch, G. W. Trucks, H. B. Schlegel, G. E. Scuseria, M. A. Robb, J. R. Cheeseman, G. Scalmani, V. Barone, G. A. Petersson, H. Nakatsuji, X. Li, M. Caricato, A. V. Marenich, J. Bloino, B. G. Janesko, R. Gomperts, B. Mennucci, H. P. Hratchian, J. V. Ortiz, A. F. Izmaylov, J. L. Sonnenberg, D. Williams-Young, F. Ding, F. Lipparini, F. Egidi, J. Goings, B. Peng, A. Petrone, T. Henderson, D. Ranasinghe, V. G. Zakrzewski, J. Gao, N. Rega, G. Zheng, W. Liang, M. Hada, M. Ehara, K. Toyota, R. Fukuda, J. Hasegawa, M. Ishida, T. Nakajima, Y. Honda, O. Kitao, H. Nakai, T. Vreven, K. Throssell, J. J. A. Montgomery, J. E. Peralta, F. Ogliaro, M. J. Bearpark, J. J. Heyd, E. N. Brothers, K. N. Kudin, V. N. Staroverov, T. A. Keith, R. Kobayashi, J. Normand, K. Raghavachari, A. P. Rendell, J. C. Burant, S. S. Iyengar, J. Tomasi, M. Cossi, J. M. Millam, M. Klene, C. Adamo, R. Cammi, J. W. Ochterski, R. L. Martin, K. Morokuma, O. Farkas, J. B. Foresman and D. J. Fox, *Gaussian 16, revision C.01*, 2016.
41 E. Vanquelef, S. Simon, G. Marquant, E. Garcia, G. Klimerak, J. C. Delepine, P. Cieplak and F.-Y. Dupradeau, *Nucleic Acids Res.*, 2011, **39**, W511–W517.
42 J. Wang, R. M. Wolf, J. W. Caldwell, P. A. Kollman and D. A. Case, *J. Comput. Chem.*, 2004, **25**, 1157–1174.
43 W. L. DeLano, *CCP4 Newsl. Protein Crystallogr.*, 2002, **40**, 82–92.
44 D. A. Case, H. M. Aktulga, K. Belfon, I. Y. Ben-Shalom, J. T. Berryman, S. R. Brozell, D. S. Cerutti, T. E. Cheatham, III, G. A. Cisneros, V. W. D. Cruzeiro, T. A. Darden, R. E. Duke, G. Giambasu, M. K. Gilson, H. Gohlke, A. W. Goetz, R. Harris, S. Izadi, S. A. Izmailov, K. Kasavajhala, M. C. Kaymak, E. King, A. Kovalenko, T. Kurtzman, T. S. Lee, S. LeGrand, P. Li, C. Lin, J. Liu, T. Luchko, R. Luo, M. Machado, V. Man, M. Manathunga, K. M. Merz, Y. Miao, O. Mikhailovskii, G. Monard, H. Nguyen, K. A. O'Hearn, A. Onufriev, F. Pan, S. Pantano, R. Qi, A. Rahnamoun, D. R. Roe, A. Roitberg, C. Sagui, S. Schott-Verdugo, A. Shajan, J. Shen, C. L. Simmerling, N. R. Skrynnikov, J. Smith, J. Swails, R. C. Walker, J. Wang, J. Wang, H. Wei, R. M. Wolf, X. Wu, Y. Xiong, Y. Xue, D. M. York, S. Zhao and P. A. Kollman, *Amber2022*, University of California, San Francisco, 2022.
45 J. D. Schmit, N. L. Kariyawasam, V. Needham and P. E. Smith, *J. Chem. Theory Comput.*, 2018, **14**, 1823–1827.
46 V. Kräutler, W. F. van Gunsteren and P. H. Hünenberger, *J. Comput. Chem.*, 2001, **22**, 501–508.
47 R. L. Davidchack, R. Handel and M. Tretyakov, *J. Chem. Phys.*, 2009, **130**, 234101.
48 H. J. C. Berendsen, J. P. M. Postma, W. F. van Gunsteren, A. DiNola and J. R. Haak, *J. Chem. Phys.*, 1984, **81**, 3684–3690.
49 J. D. Chai and M. Head-Gordon, *Phys. Chem. Chem. Phys.*, 2008, **10**, 6615–6620.
50 F. Weigend, *Phys. Chem. Chem. Phys.*, 2006, **8**, 1057–1065.
51 J. Tomasi, B. Mennucci and E. Cancès, *J. Mol. Struct.: THEOCHEM*, 1999, **464**, 211–226.
52 T. Yanai, D. P. Tew and N. C. Handy, *Chem. Phys. Lett.*, 2004, **393**, 51–57.
53 A. V. Marenich, C. J. Cramer and D. G. Truhlar, *J. Phys. Chem. B*, 2009, **18**, 6378–6396.
54 M. Caricato, B. Mennucci, J. Tomasi, F. Ingrosso, R. Cammi, S. Corni and G. Scalmani, *J. Chem. Phys.*, 2006, **124**, 124520.
55 C. Wang, Q. Qiao, W. Chi, J. Chen, W. Liu, D. Tan, S. McKechnie, D. Lyu, X. F. Jiang, W. Zhou, N. Xu, Q. Zhang, Z. Xu and X. Liu, *Angew. Chem., Int. Ed.*, 2020, **59**, 10160–10172.
56 F. Ormeno and I. J. General, *Commun. Chem.*, 2024, **7**, 26.
57 G. Jiang, Y. Ma, J. Ding, J. Liu, R. Liu and P. Zhou, *Chem. – Eur. J.*, 2023, **29**, e202300625.

Open Access Article. Published on 01 2568. Downloaded on 1/6/2569 14:33:01.
This article is licensed under a Creative Commons Attribution 3.0 Unported Licence.

58 Y. W. Tang, J. H. Wang, Q. Y. Xie, Q. Wang and J. Y. Wu, *IUCrData*, 2016, **1**, x161847.
59 V. B. Tsvetkov, A. M. Varizhuk, G. E. Pozmogova, I. P. Smirnov, N. A. Kolganova and E. N. Timofeev, *Sci. Rep.*, 2015, **5**, 16337.
60 I. Russo Krauss, A. Merlino, A. Randazzo, E. Novellino, L. Mazzarella and F. Sica, *Nucleic Acids Res.*, 2012, **40**, 8119–8128.
61 V. Van Meervelt, M. Soskine and G. Maglia, *ACS Nano*, 2014, **8**, 12826–12835.
62 K. Padmanabhan and A. Tulinsky, *Acta Crystallogr., Sect. D: Biol. Crystallogr.*, 1996, **52**, 272–282.
63 L. Chen, X. Wu, H. Yu, L. Wu, Q. Wang, J. Zhang, X. Liu, Z. Li and X. F. Yang, *Anal. Chem.*, 2021, **93**, 14343–14350.
64 R. E. Johnson, A. Pounder, J. van der Zalm, A. Chen, I. J. Bell, T. J. Van Raay, S. D. Wetmore and R. A. Manderville, *Anal. Chem.*, 2024, **96**, 16252–16259.
65 K. T. Regan, A. Pounder, C. Lin, L. D. Chen and R. A. Manderville, *J. Phys. Chem. A*, 2023, **127**, 8365–8373.
66 R. Tao, N. Wang, T. Shen, Y. Tan, Y. Ren, W. Wei, M. Liao, D. Tan, C. Tang, N. Xu, H. Wang, X. Liu and X. Li, *Theranostics*, 2022, **12**, 2549–2559.
67 C. Wang, W. Jiang, D. Tan, L. Huang, J. Li, Q. Qiao, P. Yadav, X. Liu and Z. Xu, *Chem. Sci.*, 2023, **14**, 4786–4795.
68 R. Miao, J. Li, C. Wang, X. Jiang, Y. Gao, X. Liu, D. Wang, X. Li, X. Liu and Y. Fang, *Adv. Sci.*, 2022, **9**, e2104609.
69 S. A. A. Abedi, W. Chi, D. Tan, T. Shen, C. Wang, E. C. X. Ang, C. H. Tan, F. Anariba and X. Liu, *J. Phys. Chem. A*, 2021, **125**, 8397–8403.
70 M. J. Voegtle and J. M. Dawlaty, *J. Am. Chem. Soc.*, 2022, **144**, 8178–8184.
71 S. F. Alamudun, K. Tanovitz, L. Espinosa, A. Fajardo, J. Galvan and A. S. Petit, *J. Phys. Chem. A*, 2021, **125**, 13–24.
72 S. F. Alamudun, K. Tanovitz, A. Fajardo, K. Johnson, A. Pham, T. Jamshidi Araghi and A. S. Petit, *J. Phys. Chem. A*, 2020, **124**, 2537–2546.
73 E. W. Driscoll, J. R. Hunt and J. M. Dawlaty, *J. Phys. Chem. A*, 2017, **121**, 7099–7107.
74 J. R. Hunt and J. M. Dawlaty, *J. Phys. Chem. A*, 2018, **122**, 7931–7940.
75 E. W. Driscoll, J. R. Hunt and J. M. Dawlaty, *J. Phys. Chem. Lett.*, 2016, **7**, 2093–2099.

 This journal is © the Owner Societies 2025